

Article

Crystallography and Interface Structures in As-Arc Melted and Laser Surface-Remelted Aluminum–Silicon Alloys with and without Strontium Addition

Bibhu P. Sahu ^{1,2,*} , Mohsen T. Andani ^{1,3}, Arkajit Ghosh ¹ , Jian Wang ⁴  and Amit Misra ^{1,5,*}

¹ Department of Materials Science and Engineering, University of Michigan, Ann Arbor, MI 48109, USA
² Department of Materials Science & Engineering, Texas A&M University, College Station, TX 77843, USA
³ Department of Mechanical Engineering, Texas A&M University, College Station, TX 77843, USA
⁴ Mechanical and Materials Engineering, University of Nebraska-Lincoln, Lincoln, NE 68588, USA
⁵ Department of Mechanical Engineering, University of Michigan, Ann Arbor, MI 48109, USA
* Correspondence: bibhu.igit@gmail.com (B.P.S.); amitmis@umich.edu (A.M.)

Abstract: The crystallography of the eutectic Al-Si microstructure in both unmodified and Sr (0.2 wt.%) -modified hypereutectic Al-20 wt.% Si alloys, processed via arc-melting and laser surface remelting, has been comprehensively characterized using transmission electron microscopy and electron diffraction. Although, under as-cast conditions, specific orientations between different planes of Al and Si, satisfying defined orientation relationships (ORs), have been investigated within the flake morphology, the rapid solidification induced by laser surface remelting results in a notable transformation from a flake morphology to nanocrystalline Si fibers dispersed in an Al matrix. Consequently, this transformation results in a mis-orientation of the interface between the eutectic Al and Si phases, preventing the formation of orientation relationships, thus promoting the formation of faceted interfaces exhibiting substantial lattice disregistry.

Keywords: laser surface remelting of Al-20 wt.%Si and Al-20 wt.%Si-0.2 wt.%Sr; Al-Si fiber microstructure; crystallographic orientation relationship



Citation: Sahu, B.P.; Andani, M.T.; Ghosh, A.; Wang, J.; Misra, A. Crystallography and Interface Structures in As-Arc Melted and Laser Surface-Remelted Aluminum–Silicon Alloys with and without Strontium Addition. *Crystals* **2024**, *14*, 283. <https://doi.org/10.3390/cryst14030283>

Academic Editor: Hongbin Bei

Received: 24 February 2024

Revised: 12 March 2024

Accepted: 14 March 2024

Published: 18 March 2024



Copyright: © 2024 by the authors. Licensee MDPI, Basel, Switzerland. This article is an open access article distributed under the terms and conditions of the Creative Commons Attribution (CC BY) license (<https://creativecommons.org/licenses/by/4.0/>).

1. Introduction

Aluminum–silicon (Al-Si) alloys find extensive applications across, for example, automotive, aerospace, electronics, power generation, construction, and sports industries due to their lightweight nature, good mechanical properties, and corrosion resistance [1–4]. Eutectic Si in conventionally cast Al-Si alloys exhibits the form of branched clusters of plates or flakes, known as a wheetshaeaf configuration [5]. Individual Si flakes in such an assembly exhibit internal {111} twins, which grow parallel to the flake surface. It is generally accepted that the internal twins in the flake grow at the re-entrant edge along the $\langle 112 \rangle_{\text{Si}}$ growth direction according to the twin plane re-entrant edge (TPRE) growth mechanism [5,6]. Lie et al. [7] reported that the planar isotropic growth of eutectic Si becomes anisotropic as, during the growth process, Si crystals extend in three possible co-planar $\langle 110 \rangle$ directions leading to the formation of equilateral plates. Quenching has an important effect in affecting the morphology of the eutectic Si phase. Pierantoni et al. [8] used laser surface remelting (LSR) in cast Al–Si alloys of different compositions and demonstrated a fine-scale, fibrous eutectic Si microstructure with the smallest eutectic spacing being 45 nm at the maximum growth velocity of 6.5 cm/s. The flake–fiber transition in eutectic Si morphology requires higher undercooling to achieve a finite growth rate by maintaining the zigzag-faceted interface [9].

Another way of modifying the eutectic Si morphology, which has been the subject of research over the past decades, is through the addition of certain elements in trace amounts (chemical modification). According to a review of the literature, a common approach to

modifying the eutectic Si morphology from coarse flakes to fibrous is through the addition of chemical modifiers, such as micro-alloying with Ba, Na, Ca, Sr, and rare earth elements (Ce, Y, Yb, Sc, La, Eu, etc.) at a ppm level [10–22]. Lu and Hellawell [23] introduced the impurity-induced twinning (IIT) theory, which postulates that impurity atoms absorb onto growing {111} planes, which promotes the formation of multiple twins on the same plane. In Al-Si alloys (without chemical modifiers) processed by the LSR technique, the resulting micro- or nano-scale microstructure is predominantly dependent on the growth mode which is controlled by the laser scanning parameters with internal growth twins in Si nanofibers [24,25]. Adding strontium to aluminum–silicon alloys induces significant morphological changes in the eutectic silicon. This results in an increase in the eutectic volume fraction, which enhances the strength, ductility, corrosion resistance, and thermal conductivity of the alloys. These advantageous properties make strontium-modified Al-Si alloys highly desirable for a variety of practical applications, including the aerospace industry, electronic packaging, sporting goods, and marine applications [26–29].

In addition to the eutectic morphology and twin structure in the Si phase, another important consideration in the Al-Si eutectic microstructure is the crystallographic orientation relationship (OR) between the Al and Si phase. Shamsuzzoha et al. [5] reported two ORs: $\{102\}_{Al} // \{111\}_{Si}$; $\langle 211 \rangle_{Al} // \langle 110 \rangle_{Si}$ and $\{012\}_{Al} // \{111\}_{Si}$; $\langle 110 \rangle_{Al} // \langle 110 \rangle_{Si}$ that exist in as-cast eutectic Al-12.7 wt.% Si flakes. However, Wang et al. [30] argued that Sr addition leads to a complete random orientation of nanofibrous eutectic Si, while melt-spun Al-12%Si without Sr exhibits both random orientation and a certain orientation relationship between the nano-scale Si and the α -Al.

Hypereutectic LSR Al-20Si and Al-20Si-0.2Sr alloys exhibited high flow strength and plastic deformability at room temperature [31]. However, the simultaneous effect of the rapid cooling rate in laser solidification and chemical modification on the crystallographic orientation relationship between the Al and Si phase in eutectic microstructures has not been investigated in detail. The purpose of this research is to systematically study the OR between the Al and Si eutectic phases in as-arc melted and laser surface-remelted conditions with nano-fibrous Si morphology in hyper-eutectic Al-Si alloys with and without Sr modification.

2. Experimental Procedures

Sr-modified (0.2 wt.%) and unmodified Al-20 wt.% Si hypereutectic alloys were prepared by vacuum arc melting. Several rectangular pieces with dimensions 20 mm (length: L) \times 10 mm (width: W) \times 5 mm (thickness: T) were cut out of the as-cast alloys received in button form. The top surfaces were ground with 120-grit SiC sandpaper to 3 μ m surface roughness in order to ensure maximum laser absorption and a uniform melt pool microstructure throughout the scanning track [24]. The LSR parameters were chosen to cover a wide range of power densities, leading to the adoption of Taguchi's experimental design method. This approach facilitated a straightforward comparison of key outputs, including the area of fully eutectic regions, the area fraction of fully eutectic regions relative to the entire melt pool, the width and depth of the melt pool, and the cooling rates of the processed material. LSR was performed on the ground surface of the alloys placed on a stainless steel substrate, employing laser power, spot diameter, and scanning velocity at 200 W, 75 μ m, and 100 mm/s, respectively. Laser scanning was carried out using the Open Additive PANDATM machine. The top surfaces of the blocks were not coated with absorbent material in order to mitigate the formation of extraneous phases and to make this approach leaner for future applications.

Both low-magnification and high-resolution modes in Transmission Electron Microscopy (TEM), as well as scanning transmission electron microscopy (STEM) characterization, were conducted using a Thermo Fisher Talos F200X G2 S/TEM (Thermo Fisher Scientific Inc., Waltham, MA, USA). The primary objective was to characterize the eutectic Al-Si microstructure, with a specific focus on evaluating the orientation relationship between the two phases. This was achieved using the Selected Area Diffraction (SAD)

aperture coupled with the TEM mode, allowing for a detailed and comprehensive structural analysis. TEM specimens were prepared by focused ion beam (FIB) milling using a Nova 200 Nanolab and a Helios G4 Plasma FIB UXe SEM/FIB (Thermo Fisher Scientific Inc., Waltham, MA, USA) for foil lift-out and thinning to electron transparency, respectively. A protective Pt surface cap was deposited in two steps. Firstly, a 0.5 μm thick cap was deposited using the electron beam at 5 kV and 1.6 nA. Following this, a thicker 2 μm cap was deposited using the Ga⁺ ion Focused Ion Beam (FIB) at 30 kV and 80 pA. Lift-outs with dimensions of 15 μm \times 2 μm \times 2.5 μm (length \times width \times height) were then cut using the FIB and attached to Cu TEM half-grids. Initial thinning of the sample was performed on the Helios 650 using FIB parameters of 30 kV and 1 nA, followed by 30 kV and 0.1 nA. Final thinning was achieved using a Thermo Fisher Helios G4 Plasma FIB UXe dual-beam Scanning Electron Microscope/FIB (SEM/FIB) (Thermo Fisher Scientific Inc., Waltham, MA, USA). The PFIB parameters employed were 30 kV and 30 pA until the sample reached a thickness of approximately 100 nm, followed by 30 kV and 10 pA until the sample became electron transparent. A final cleaning polish was carried out at 5 kV and 100 pA to ensure the sample was prepared appropriately for further analysis.

3. Results

Figure 1a shows the BF STEM image of the micron-size eutectic Si flake located in the α -Al matrix in the as-cast Al-20Si, whereas Figure 1b demonstrates the SAD pattern from the selected region, A, considering the interface of the Al and Si phases. The diffraction pattern shows an electron beam direction //Al[001]//Si[011] (in Figure 1b) and, within these zones, ($\bar{1}20$)Al//($\bar{1}1\bar{1}$)Si. This SAD pattern is consistent with the OR, {120}Al//{111}Si and $\langle 001 \rangle$ Al// $\langle 011 \rangle$ Si, reported by Shamsuzzoha and Hogan in Al-12.7 wt.% Si eutectic alloys [5].

Similarly, Figure 1c,d shows the BF STEM image of the as-cast Al-20Si-0.2Sr eutectic alloy and the corresponding SAD pattern from the marked circle B, respectively. The diffraction pattern indicates an electron beam direction of //Al[001]//Si[001] with a 45° rotation of about [001], thus the OR is (020)Al//($\bar{2}20$)Si and ($\bar{2}20$)Al//($\bar{2}00$)Si, which is different from the one above for the unmodified as-cast Al-Si. On the contrary, Shamsuzzoha et al. [32] observed that the aluminum phase in the strontium-modified eutectic develops as elongated columnar grains parallel to the silicon fibers, exhibiting a pronounced $\langle 110 \rangle$ fiber texture. Nevertheless, no consistent orientation relationship was identified between the silicon and aluminum phases.

The results indicate that the rapid solidification involved in laser surface remelting leads to the transformation of the micron-sized flake morphology of the eutectic Si to nanocrystalline Si fibers embedded in an Al matrix. Different sets of ORs were observed in LSR-fabricated nano-eutectic Al-20Si and Al-20Si-0.2Sr alloys, as depicted in Figure 2. The dark region in Figure 2a indicates one Al colony tilted to the Al[$\bar{1}11$] zone axis. Further, Figure 2b represents the corresponding SAD pattern from the location, A, within the same Al colony. In location A, the beam direction is parallel to Al[$\bar{1}11$]//Si[$\bar{1}\bar{1}2$] with one set of parallel planes of ($12\bar{1}$)Al//($\bar{1}\bar{1}1$)Si. These results are consistent with the OR, {112}Al//{111}Si and $\langle 111 \rangle$ Al// $\langle 112 \rangle$ Si, reported by Lien et al. [24]. Further, there is a mis-orientation of 7° between the Al($\bar{2}0\bar{2}$) and Si(220) planes, as seen in Figure 2b.

The marked location, A, within the dark region in Figure 3a represents the TEM micrograph of one Al-Si colony tilted to the Al[$\bar{1}\bar{1}2$] zone axis in the LSR Al-20Si-0.2Sr nanoeutectic alloy. The SAD pattern shown in Figure 3b reveals that the Al matrix and the nano-sized Si fibers are oriented along the Al[$\bar{1}\bar{1}2$] and Si[$\bar{1}\bar{1}2$] zone axis, demonstrating a mis-orientation of 12° between the corresponding planes while satisfying the zone axis of [$\bar{1}\bar{1}2$]. Similarly, another Al-Si colony in the LSR Al-20Si-0.2Sr nanoeutectic alloy tilted to the $\langle 011 \rangle$ beam direction of the Al phase is presented in Figure 3c and the corresponding SAD pattern shown in Figure 3d indicates the presence of {111} and {200} planes of Al following the $\langle 011 \rangle$ zone axis. In contrast, the appearance of ($\bar{1}\bar{1}\bar{1}$) and ($13\bar{1}$) planes of the Si fibers in the diffraction pattern (Figure 3d) does not confirm any preferred OR within the

Al planes. This observation suggests a predominantly random orientation of the Si fibers within the Al matrix. All the possible pairs of ORs observed in both the as-cast and LSR conditions in the present study are listed in Table 1.

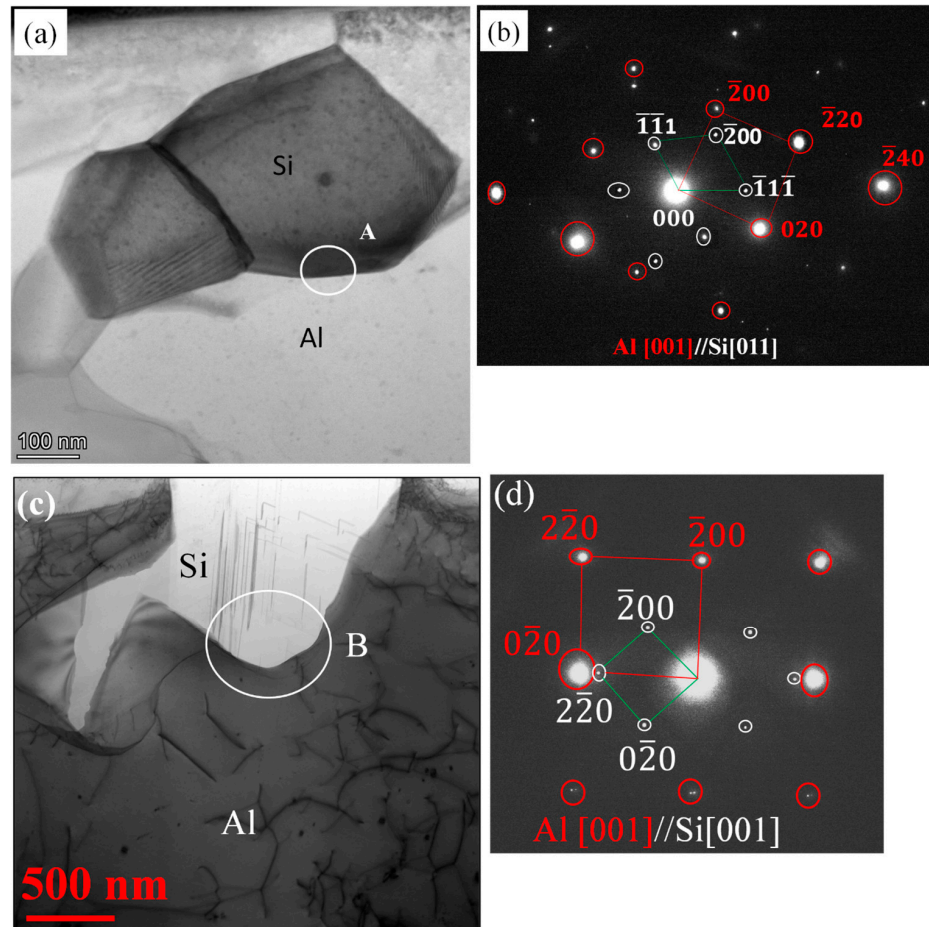


Figure 1. (a) BF STEM image of the as-cast Al-20Si alloy, (b) SAD pattern from the highlighted region, A, (c) BF STEM image of the as-cast Al-20Si-0.2Sr alloy, and (d) SAD pattern from the highlighted region, B.

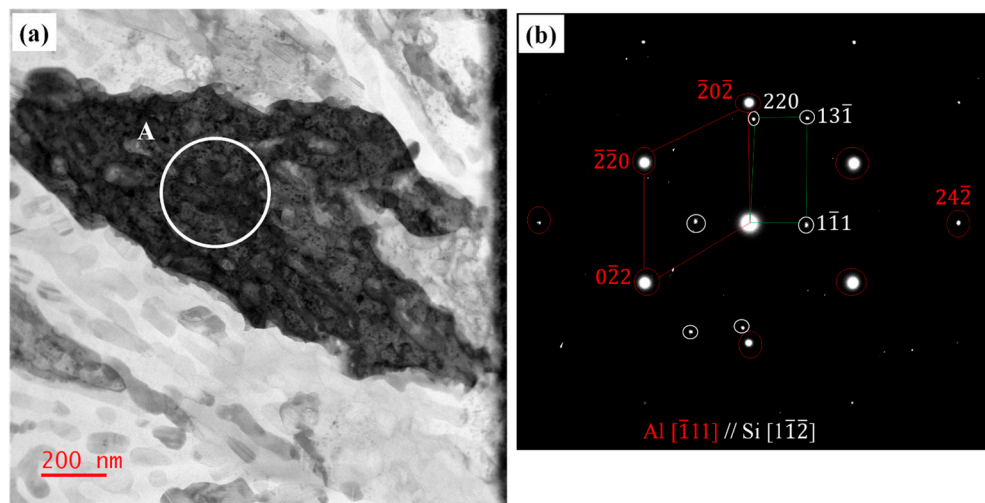


Figure 2. LSR Al-20Si: (a) BF STEM image showing one Al-Si colony (dark region) tilted to the Al$\langle 1\bar{1}1 \rangle$ zone axis and (b) SAD pattern from the location, A. Red lines indicate the indexing the Al phase and white lines indicate the indexing the Si phase in (b).

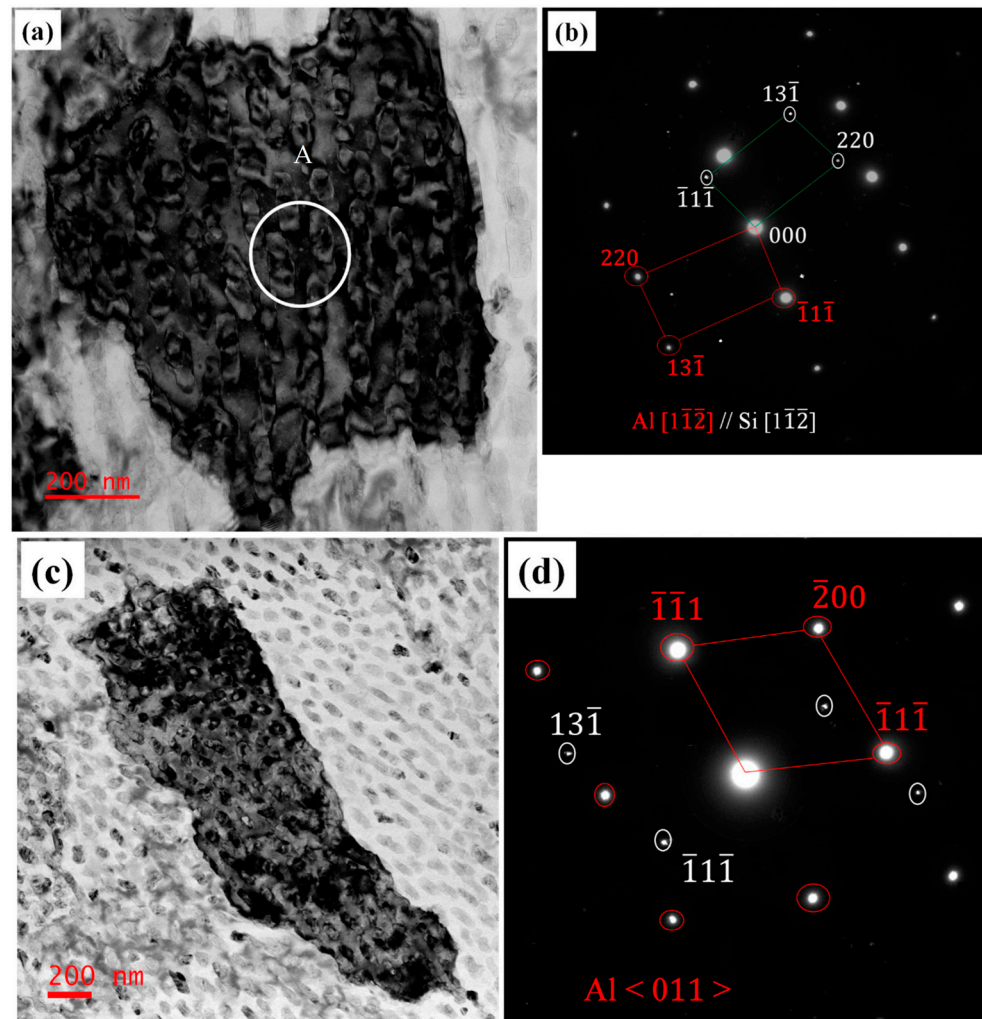


Figure 3. LSR Al-20Si-0.2Sr: (a) BF STEM image showing one Al-Si colony (dark region) tilted to the Al<111> zone axis, (b) SAD pattern from the location, A, (c) BF STEM image showing another Al-Si colony (dark region) tilted to the Al<011> zone axis, and (d) corresponding diffraction pattern.

Table 1. Crystallographic orientation relationships observed in Al-20Si and Al-20Si-0.2Sr in both as-cast and LSR conditions, in comparison with the literature.

Alloy Type	Parallel Direction	Parallel Planes
As-cast Al-Si eutectic (Si flake) (Present study)	Al<001> // Si<011>	{012}Al // {111}Si
As-cast Al-Si eutectic (Si flake) [5]	Al<211> // Si<110>	{102}Al // {111}Si
	Al<100> // Si<110>	{012}Al // {111}Si
As-cast Al-Si-Sr eutectic (Si flake) (Present study)	Al<001> // Si<001>	{020}Al // {220}Si {220}Al // {200}Si
LSR Al-20Si nanoeutectic (Si nanofibers) (Present study)	Al<111> // Si<112>	{112}Al // {111}Si
LSR Al-20Si nanoeutectic (Si nanofibers) [24]	Al<111>Al // Si<112>	{112}Al // {111}Si
LSR Al-20Si-0.2Sr nanoeutectic (Si nanofibers) (Present study)	Al<112> // Si<112>	12° mis-orientation between {113}Al and {113}Si, {111}Al and {111}Si, {220}Al and {220}Si

Moreover, the local OR and interface habit planes between the Si fibers and the Al matrix in the case of an LSR Al-20Si alloy is explained through HRSTEM imaging and fast Fourier Transform (FFT). Figure 4a illustrates a high-magnification view of a eutectic Si fiber embedded within the Al matrix. Meanwhile, Figure 4b provides a high-resolution

image of the interface denoted by the dotted square in Figure 4a. The corresponding FFT pattern reveals that the Al phase is oriented along the [011] beam direction. However, the diffraction spots from the Si phase correspond to several planes without satisfying any particular zone axis, indicating no preferred OR between the Al and Si.

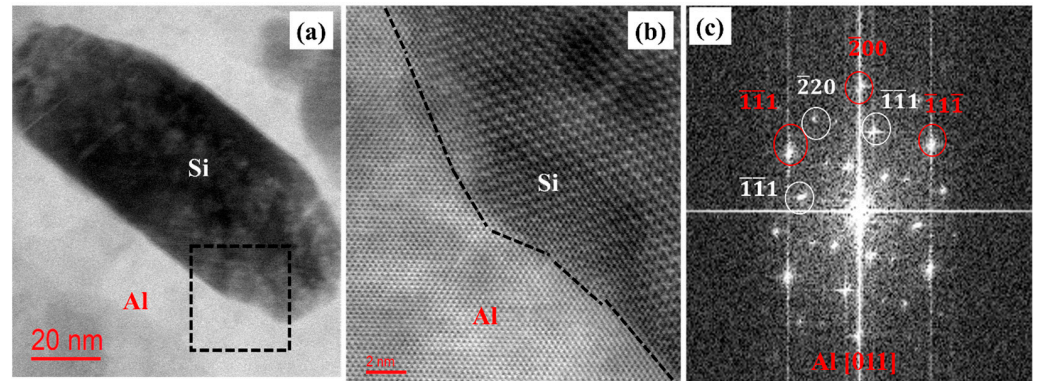


Figure 4. (a) STEM image showing one Si fiber in the Al matrix in the LSR Al-20Si alloy, (b) HRTEM image of the interface indicated by the black dotted lines from the marked square in (a), and (c) the FFT pattern showing along the Al<011> beam direction, whereas the Si fiber does not satisfy any zone axis.

Additionally, a magnified view of the Al-Si eutectic microstructure in the case of LSR Al-20Si-0.2Sr is shown in Figure 5a, whereas one of the local interfaces highlighted by the dotted square is further enlarged in Figure 5b, focusing on the Al-Si interface-oriented edge with both crystals diffracting. The micrograph in Figure 5b represents a faceted interface between one Si fiber and the Al matrix, indicating a semi-coherent type. The Si phase is oriented along the <011> beam direction, whereas the Al phase is not on the zone axis, as indicated by FFT, since not all Al spots are present (Figure 5b). An analysis of the FFT (Figure 5c) confirmed a slight mis-orientation between the Al(111) plane and Si(111) plane ($\sim 10^\circ$) from the zone axes of <011>Al and <011>Si.

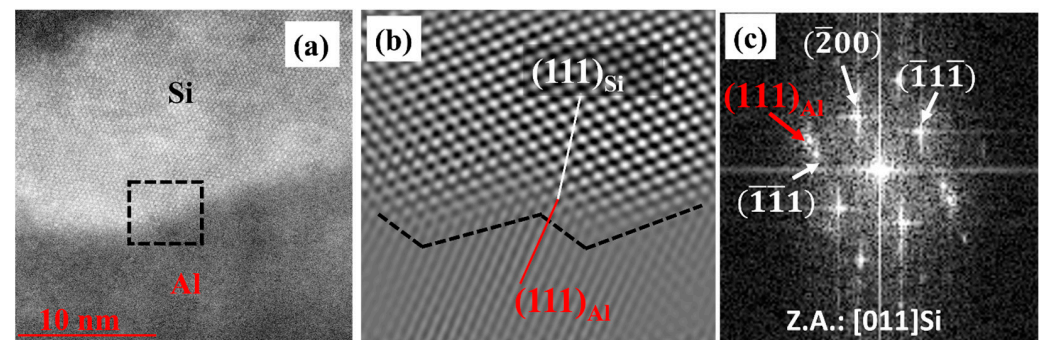


Figure 5. (a) STEM image showing one Si fiber in the Al matrix in the LSR Al-20Si-0.2Sr alloy, (b) BF HRSTEM image showing a faceted interface between the (111)Al and (111)Si plane captured from the marked location in (a), and (c) The corresponding FFT pattern oriented along the [011]Si zone axis, whereas the diffraction pattern of Al does not follow any zone axis. The black dotted lines in (b) indicate the interface.

4. Discussion

In the case of as-cast Al-Si and Al-Si-Sr alloys, our study confirms the OR of <001>Al//<011>Si and {012}Al//{111}Si and the OR of <001>Al//<001>Si and {010}Al//{110}Si, respectively (Table 1). The stereographic projections and atom models generated using Vesta software (Version: 3.4.5) have been employed to elucidate the orientation relationship between various crystallographic planes, thereby corroborating

the experimental observations. The stereographic projections following the parallel beam directions of ORs $\langle 001 \rangle_{\text{Al}} // \langle 011 \rangle_{\text{Si}}$ observed in the as-cast Al-20Si eutectic alloy are shown Figure 6a. The atom models representing the $\{012\}_{\text{Al}}$ (left side denoted by red color atoms) and $\{111\}_{\text{Si}}$ (right side denoted by blue color atoms) planes are shown in Figure 6b. The boundary plane looking down from the $\{012\}_{\text{Al}} // \{111\}_{\text{Si}}$ plane is shown in Figure 6c.

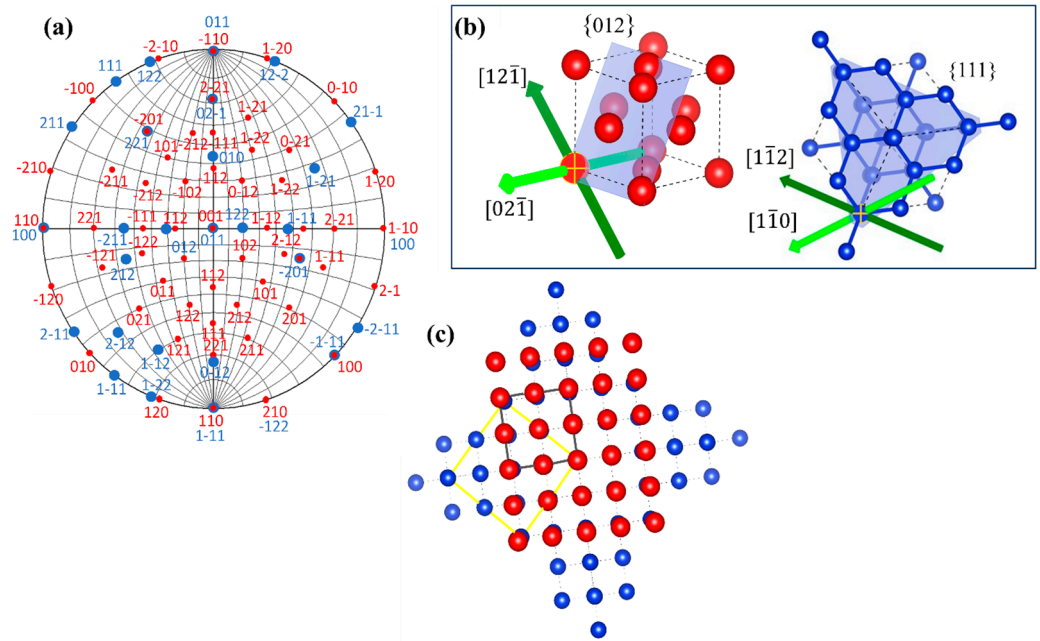


Figure 6. As-cast Al-20Si alloy: (a) stereographic projection along the $[001]_{\text{Al}} // [011]_{\text{Si}}$ direction, (b) Atom models highlighting the $\{012\}_{\text{Al}}$ (left side denoted by red color atoms) and $\{111\}_{\text{Si}}$ (right side denoted by blue color atoms) planes, and (c) interface plane looking down from $\{012\}_{\text{Al}} // \{111\}_{\text{Si}}$.

Figure 7a represents the stereographic projection following the parallel beam directions of ORs $\langle 001 \rangle_{\text{Al}} // \langle 001 \rangle_{\text{Si}}$ observed in the as-cast Al-20Si-0.2Sr eutectic alloy with a Si flake morphology. The atom models representing the $\{100\}_{\text{Al}}$ (left side denoted by red color atoms) and $\{100\}_{\text{Si}}$ (right side denoted by blue color atoms) planes are shown in Figure 7b. The corresponding boundary plane looking down from the $\{100\}_{\text{Al}} // \{100\}_{\text{Si}}$ plane is shown in Figure 7c, which has been observed in the SAD pattern shown in Figure 1d. Further, according to the OR of the $\langle 001 \rangle_{\text{Al}} // \langle 001 \rangle_{\text{Si}}$ beam direction, other sets of parallel planes are Al $\{110\}$ and Si $\{110\}$ and the corresponding atom models indicating these planes are represented in Figure 7d. The boundary plane looking down from the parallel planes of Al $\{110\}$ and Si $\{110\}$ is shown in Figure 7e. The stereographic projection drawn of the OR Al $\{111\} // \text{Si}\{112\}$ beam direction drawn for the LSR nanoeutectic Al-20Si alloy is shown in Figure 8a. The atom models of the parallel planes along this beam direction are shown in Figure 8b–d. The boundary planes looking down from $\{112\}_{\text{Al}} // \{111\}_{\text{Si}}$ and Al $\{001\} // \text{Si}\{110\}$ are represented in Figure 8e,f, respectively. The stereographic projection drawn of the OR Al $\langle 112 \rangle // \text{Si}\langle 112 \rangle$ beam direction drawn for the LSR nanoeutectic Al-20Si-0.2Sr alloy is shown in Figure 9a. The atom models of the parallel planes of Al $\{111\}$ and Si $\{111\}$ along this beam direction are shown in Figure 9b. The boundary planes looking down from the Al $\{111\} // \text{Si}\{111\}$ plane are represented in Figure 9c.

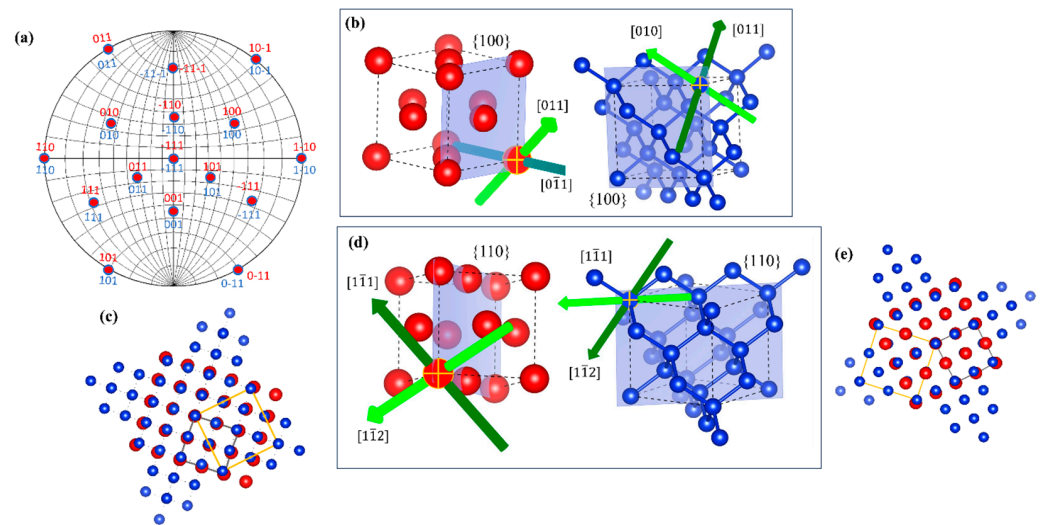


Figure 7. As-cast Al-20Si-0.2Sr alloy: (a) stereographic projection along the [001]Al // [001]Si direction, (b) atom models highlighting the {100}Al (left side denoted by red color atoms) and {100}Si (right side denoted by blue color atoms) planes, (c) corresponding interface plane looking down from {100}Al // {100}Si, (d) atom planes showing Al{110} and Si{110} planes, and (e) corresponding interface plane looking down from {110}Al // {110}Si.

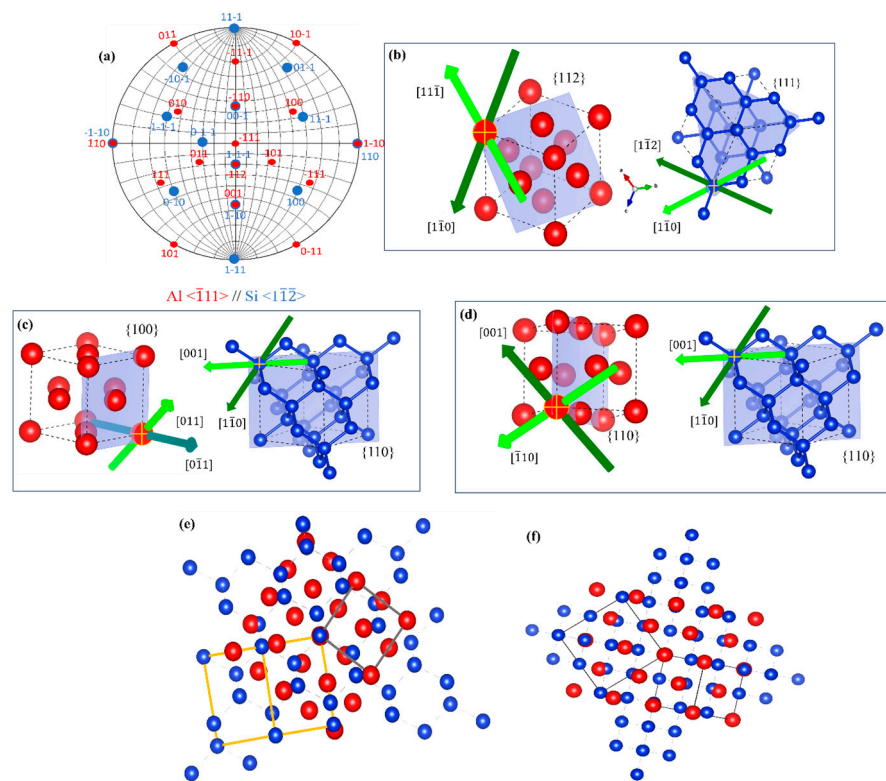


Figure 8. LSR Al-20Si alloy: (a) stereographic projection along the Al<111> // Si<112> direction, (b) atom models highlighting the {112}Al (left side denoted by red color atoms) and {111}Si (right side denoted by blue color atoms) planes, (c) {001}Al (left side denoted by red color atoms) and {110}Si (right side denoted by blue color atoms) planes, (d) {110}Al (left side denoted by red color atoms) and {110}Si (right side denoted by blue color atoms) planes, (e) interface plane looking down from {112}Al // {111}Si, and (f) interface plane looking down from {001}Al // {110}Si.

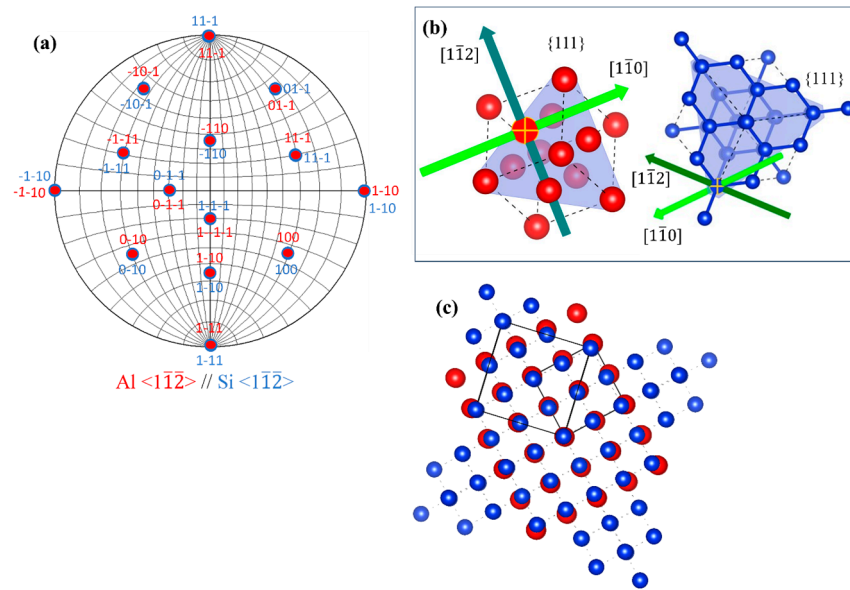


Figure 9. LSR Al-20Si-0.2Sr: (a) stereographic projection along the $\langle 11\bar{2} \rangle_{Al} // \langle 11\bar{2} \rangle_{Si}$ direction, (b) atom models highlighting the $\{111\}_{Al}$ (left side denoted by red color atoms) and $\{111\}_{Si}$ (right side denoted by blue color atoms) planes, and (c) interface plane looking down from $\{111\}_{Al} // \{111\}_{Si}$.

The results reveal distinct types of ORs between the Al and Si phases in Al-20Si and Al-20-0.2Sr alloys under both as-cast and LSR conditions, implying that the ORs are independent of both the processing conditions and the inclusion of modifiers. For rapid solidification in the laser surface melting process, the growth kinetics effect could play a dominant role in the eutectic Al-Si microstructure with large fusion entropy and strong growth anisotropy [32]. A detailed analysis of the OR of the Al-Si eutectic local interface (Figure 7a) reveals a semi-coherent faceted interface between the zone axis of the $\langle 001 \rangle_{Al} // \langle 001 \rangle_{Si}$ interface. The corresponding FFT confirms that the (111) plane of Al is mis-oriented at an angular tilt of 10° with the (111) plane of Si. We applied the Bramfitt planar disregistry to reveal the evolution of these two crystallographic relationships [33]:

$$\delta_{(111)_{Si}}^{(111)_{Al}} = \frac{1}{3} \sum_{i=1}^3 \frac{d_{(111)_{Al}} \cos \theta - d_{(111)_{Si}}}{d_{(111)_{Si}}} \quad (1)$$

where the $d_{(111)_{Al}}$ and $d_{(111)_{Si}}$ are the d -spacings of the (111) and (111) planes of Al and Si, respectively, and θ is the mis-orientation angle. The planar disregistry value (δ) was calculated to be 20%, which confirms the higher interface energy between the (111) plane of Al and the (111) plane of Si, leading to the formation of semi-coherent faceted growth. A mis-orientation angle of 17° between the (111)Al and (111)Si interface of the ultrafine eutectic region oriented along a different zone axis of $\langle 111 \rangle_{Al} // \langle 11\bar{2} \rangle_{Si}$ has been observed in laser-processed Al-20 wt.% Si [24]. This could be suggestive of the lattice mismatch due to presence of steps/ledges at the Al/Si interfaces, as well as the formation of various kinds of fault structures, such as multiple nanotwins in eutectic Si fibers. This might also be caused by the competitive effect between interfacial energy and growth kinetics due to the faster solidification rate during laser processing [34]. Wu et al. [35] simulated a bilayer of an Al and Si model with a semi-coherent (111)Al// (111)Si interface. According to the model, the semi-coherent (111)Al// (111)Si interface should contain 19 periodic units for Al and 14 periodic units for Si. The minimum interfacial strains between these sets of parallel planes can be calculated according to the relation [36]

$$\varepsilon_{x/y} = \frac{2(n_y d_x - n_x d_y)}{n_y d_x + n_x d_y} \quad (2)$$

where d_x and d_y are the interplanar spacings for the planes x and y , respectively, and m_x and n_y are the integers, according to the relation, $d_x/d_y = m_x/n_y$. In general, in the $(\bar{1}\bar{1}\bar{1})_{Al} // (\bar{1}\bar{1}\bar{1})_{Si}$ coherent interface, $d_{Al}(111) = 0.2338$ nm (PDF#00-004-0787) and $d_{Si}(111) = 0.3113$ nm (PDF#01-080-0018), so n_{Al} and n_{Si} equal 3 and 4, respectively. This means that four (111) planes of Al match with three (111) planes of Si. Using these ratios, the minimum value of lattice strains calculated using Equation (2) for two different types of Al-Si interfaces observed experimentally (Figures 7 and 8) is summarized in Table 2.

Table 2. Parameters for the calculation of the minimum lattice strains.

Parallel Planes	Interface Type	d -Spacings (nm)	n_{Al}/n_{Si}	$\epsilon_{x/y}$ (%)
(111)Al // (111)Si	Semi-coherent	$d_{Al}(111) = 0.2338$ $d_{Si}(111) = 0.3113$	19/14 [31]	1.9
$(\bar{1}\bar{1}\bar{1})_{Al} // (\bar{1}\bar{1}\bar{1})_{Si}$	Coherent	$d_{Al}(111) = 0.2338$ $d_{Si}(111) = 0.3106$	4/3	0.13

The observed crystallographic orientation relationships (ORs) between the eutectic Al and Si interfaces have profound implications for the mechanical properties of the alloy, particularly concerning the effects of coherent and incoherent boundaries. Future research will seek to deepen our understanding of the relationship between processing methods—specifically the impact of cooling rate and the addition of modifiers—on the orientation relationships among various interfaces. This research will investigate how these changes influence the material's strength, ductility, and other key mechanical characteristics. Furthermore, a key focus will be on the reproducibility of the proposed method, involving investigations into various compositions and process parameters to ensure consistent and reliable outcomes. By elucidating these relationships, we aim to optimize the processing parameters during laser surface remelting, which is expected to enhance control over the eutectic Al-Si microstructure, focusing on the crystallographic ORs, and improve the mechanical performance of the manufactured components.

5. Conclusions

The crystallographic orientation relationship between the Al and Si phases in the eutectic microstructure was investigated in both as-cast and laser-remelted conditions for Al-20Si and Al-20Si-0.2Sr alloys. The findings deviated from the values reported in the literature, indicating that the orientation relationship is not solely influenced by the processing conditions. The laser processing method, which involves rapid solidification, contributed to the formation of faceted Al-Si interfaces exhibiting local variations in the orientation relationship between the Al and Si phase. In particular, a 10° angular misorientation was measured between the (111)Al and (111)Si planes in Al-20Si-0.2Sr under LSR conditions. This angular misalignment resulted in a substantial lattice registry of 20%.

Author Contributions: B.P.S. conducted the microstructural characterization and data analysis; M.T.A. and A.G. synthesized materials. B.P.S., A.M. and J.W. prepared the manuscript. A.M. and J.W. conceived this study. All authors have read and agreed to the published version of the manuscript.

Funding: This research is sponsored by the Department of Energy, Office of Science, Office of Basic Energy Sciences (Grant No. DE-SC0016808).

Data Availability Statement: The original contributions presented in the study are included in the article; further inquiries can be directed to the corresponding author.

Acknowledgments: B.P.S. would like to thank the Michigan Center for Materials Characterization for their microstructural observation of the material.

Conflicts of Interest: The authors declare no conflicts of interest.

References

1. Pereira, C.L.; Gomes, L.F.; Garcia, A.; Spinelli, J.E. Comparing the Roles of Sb and Bi on Microstructures and Application Properties of the Al-15% Si Alloy. *J. Alloys Compd.* **2021**, *878*, 160343. [[CrossRef](#)]
2. Samuel, A.; Zedan, Y.; Doty, H.; Songmene, V.; Samuel, F.H. A Review Study on the Main Sources of Porosity in Al-Si Cast Alloys. *Adv. Mater. Sci. Eng.* **2021**, *2021*, 1921603. [[CrossRef](#)]
3. Dash, S.S.; Chen, D. A Review on Processing–Microstructure–Property Relationships of Al-Si Alloys: Recent Advances in Deformation Behavior. *Metals* **2023**, *13*, 609. [[CrossRef](#)]
4. Samal, P.; Mani Babu, D.; Kiran, S.V.; Surekha, B.; Vundavilli, P.R.; Mandal, A. Study of Microstructural and Machining Characteristics of Hypereutectic Al-Si Alloys Using Wire-EDM for Photovoltaic Application. *Silicon* **2020**, *13*, 4407–4419. [[CrossRef](#)]
5. Shamsuzzoha, M.; Hogan, L.M. Crystal Morphology of Unmodified Aluminium-Silicon Eutectic Microstructures. *J. Cryst. Growth* **1986**, *76*, 429–439. [[CrossRef](#)]
6. Shamsuzzoha, M.; Hogan, L.M.; Smith, D.J.; Deymier, P.A. A Transmission and High-Resolution Electron Microscope Study of Cozonally Twinned Growth of Eutectic Silicon in Unmodified Al-Si Alloys. *J. Cryst. Growth* **1991**, *112*, 635–643. [[CrossRef](#)]
7. Liu, X.; Zhang, Y.; Beausir, B.; Liu, F.; Esling, C.; Yu, F.; Zhao, X.; Zuo, L. Twin-Controlled Growth of Eutectic Si in Unmodified and Sr-Modified Al-12.7%Si Alloys Investigated by SEM/EBSD. *Acta Mater.* **2015**, *97*, 338–347. [[CrossRef](#)]
8. Pierantoni, M.; Gremaud, M.; Magnin, P.; Stoll, D.; Kurz, W. The Coupled Zone Of Rapidly Solidified Al-Si Alloys In Laser Treatment. *Acta Metall. Mater.* **1992**, *40*, 1637–1644. [[CrossRef](#)]
9. Mazahery, A.; Shabani, M.O. Modification Mechanism and Microstructural Characteristics of Eutectic Si in Casting Al-Si Alloys: A Review on Experimental and Numerical Studies. *JOM* **2014**, *66*, 726–738. [[CrossRef](#)]
10. Ho, C.R. Modification of Hypoeutectic Al-Si Alloys. *J. Mater. Sci.* **1995**, *30*, 1912–1920. [[CrossRef](#)]
11. Knuutinen, A.; Nogita, K.; McDonald, S.D.; Dahle, A.K. Modification of Al-Si Alloys with Ba, Ca, Y and Yb. *J. Light Met.* **2001**, *1*, 229–240. [[CrossRef](#)]
12. Lu, S.-Z.; Hellawell, A. Modification of Al-Si Alloys: Microstructure, Thermal Analysis, and Mechanisms. *JOM* **1995**, *47*, 38–40. [[CrossRef](#)]
13. Chang, J.Y.; Kim, G.H.; Moon, I.G.; Choi, C.S. Rare Earth Concentration in the Primary Si Crystal In Rare Earth added Al-21wt.%Si Alloy. *Scr. Mater.* **1998**, *39*, 307–314. [[CrossRef](#)]
14. Liang, S.M.; Schmid-Fetzer, R. Phosphorus in Al-Si Cast Alloys: Thermodynamic Prediction of the AIP and Eutectic (Si) Solidification Sequence Validated by Microstructure and Nucleation Undercooling Data. *Acta Mater.* **2014**, *72*, 41–56. [[CrossRef](#)]
15. Qiyang, L.; Qingchun, L.I. Modification Of Al-Si Alloys with Sodium. *Acta Metall. Mater.* **1991**, *39*, 2497–2502. [[CrossRef](#)]
16. Fat-Halla, N. Structural Modification of Al-Si Eutectic Alloy by Sr and its effect on Tensile and Fracture characteristics. *J. Mater. Sci.* **1989**, *24*, 2488–2492. [[CrossRef](#)]
17. Fatahalla, N.; Hafiz, M.; Abdulkhalek, M. Effect of Microstructure on the Mechanical Properties and Fracture of Commercial Hypoeutectic Al-Si Alloy Modified with Na, Sb and Sr. *J. Mater. Sci.* **1999**, *34*, 3555–3564. [[CrossRef](#)]
18. Chang, J.; Moon, I.; Choi, C. Refinement of Cast Microstructure of Hypereutectic Al-Si Alloys through the Addition of Rare Earth Metals. *J. Mater. Sci.* **1998**, *33*, 5015–5023. [[CrossRef](#)]
19. Li, J.; Hage, F.; Wiessner, M.; Romaner, L.; Scheiber, D.; Sartory, B.; Ramasse, Q.; Schumacher, P. The Roles of Eu during the Growth of Eutectic Si in Al-Si Alloys. *Sci. Rep.* **2015**, *5*, 13802. [[CrossRef](#)]
20. Nogita, K.; Drennan, J.; Dahle, A.K. Evaluation of Silicon Twinning in Hypo-Eutectic Al-Si Alloys. *Mater. Trans.* **2003**, *44*, 625–628. [[CrossRef](#)]
21. Barrirero, J.; Pauly, C.; Engstler, M.; Ghanbaja, J.; Ghafoor, N.; Li, J.; Schumacher, P.; Odén, M.; Mücklich, F. Eutectic Modification by Ternary Compound Cluster Formation in Al-Si Alloys. *Sci. Rep.* **2019**, *9*, 5506. [[CrossRef](#)]
22. Sha, X.; Chen, X.; Ning, H.; Xiao, L.; Yin, D.; Mao, L.; Zheng, J.; Zhou, H. Modification of Eutectic Si in Al-Si-(Ba) Alloy by Inducing a Novel 9R Structure in Twins. *Materials* **2018**, *11*, 1151. [[CrossRef](#)]
23. Lu, S.-Z.; Hellawell, A. The Mechanism of Silicon Modification in Aluminum-Silicon Alloys: Impurity Induced Twinning. *Metall. Trans. A* **1986**, *18*, 1721–1733. [[CrossRef](#)]
24. Lien, H.H.; Mazumder, J.; Wang, J.; Misra, A. Microstructure Evolution and High Density of Nanotwinned Ultrafine Si in Hypereutectic Al-Si Alloy by Laser Surface Remelting. *Mater. Charact.* **2020**, *161*, 110147. [[CrossRef](#)]
25. Abboud, J.; Mazumder, J. Developing of Nano Sized Fibrous Eutectic Silicon in Hypereutectic Al-Si Alloy by Laser Remelting. *Sci. Rep.* **2020**, *10*, 12090. [[CrossRef](#)]
26. Vasudevan, G.; Anbukkarasi, R.; Sanil, H.; Ravi, M. Combined Effect of Sr-Addition and Pressure Induced Solidification on Eutectic-Si Morphology and Mechanical Properties of Squeeze Cast Al-Si Binary Alloy. *Mater. Today Commun.* **2023**, *34*, 105104. [[CrossRef](#)]
27. Öztürk, İ.; Hapçı Ağaoglu, G.; Erzi, E.; Dispinar, D.; Orhan, G. Effects of Strontium Addition on the Microstructure and Corrosion Behavior of A356 Aluminum Alloy. *J. Alloys Compd.* **2018**, *763*, 384–391. [[CrossRef](#)]
28. Ganesh, M.R.S.; Reghunath, N.J.; Levin, M.; Prasad, A.; Doondi, S.; Shankar, K.V. Strontium in Al-Si-Mg Alloy: A Review. *Met. Mater. Int.* **2022**, *28*, 1–40. [[CrossRef](#)]
29. Guo, J.; Guan, Z.P.; Yan, R.F.; Ma, P.K.; Wang, M.H.; Zhao, P.; Wang, J.G. Effect of Modification with Different Contents of Sb and Sr on the Thermal Conductivity of Hypoeutectic Al-Si Alloy. *Metals* **2020**, *10*, 1637. [[CrossRef](#)]

30. Wang, Y.; Zhang, Z.; Zheng, S.; Wang, W.; Bian, X. Effect of Sr Addition on the Microstructure of a Rapidly Solidified Al-12 Wt.% Si Alloy. *Pract. Metallogr.* **2005**, *42*, 411–422. [[CrossRef](#)]
31. Ghosh, A.; Wu, W.; Sahu, B.P.; Wang, J.; Misra, A. Enabling Plastic Co-Deformation of Disparate Phases in a Laser Rapid Solidified Sr-Modified Al-Si Eutectic through Partial-Dislocation-Mediated-Plasticity in Si. *Mater. Sci. Eng. A* **2023**, *885*, 145648. [[CrossRef](#)]
32. Shamsuzzoha, M.; Hogan, L. The crystal morphology of fibrous silicon in strontium-modified Al-Si eutectic. *Philos. Mag. A* **1986**, *54*, 459–477. [[CrossRef](#)]
33. Liu, Y.; Su, H.; Shen, Z.; Zhao, D.; Guo, Y.; Li, S.; Guo, M.; Liu, L.; Fu, H. Effect of Seed Orientations on Crystallographic Texture Control in Faceted Al₂O₃/YAG Eutectic Ceramic during Directional Solidification. *J. Mater. Sci. Technol.* **2023**, *146*, 86–101. [[CrossRef](#)]
34. Fan, Z.; Zhao, Y.; Tan, Q.; Mo, N.; Zhang, M.X.; Lu, M.; Huang, H. Nanostructured Al₂O₃-YAG-ZrO₂ Ternary Eutectic Components Prepared by Laser Engineered Net Shaping. *Acta Mater.* **2019**, *170*, 24–37. [[CrossRef](#)]
35. Wu, W.; Gong, M.; Wei, B.; Misra, A.; Wang, J. Atomistic Modeling of Interface Strengthening in Al-Si Eutectic Alloys. *Acta Mater.* **2022**, *225*, 117586. [[CrossRef](#)]
36. Wang, X.; Zhong, Y.; Sun, Q.; Li, Y.; Zhang, W.; Qi, D.; Wang, D.; Jiang, B. Crystallography and Interfacial Structure in a Directionally Solidified Al₂O₃/Y₃Al₅O₁₂/ZrO₂ Eutectic Crystal. *Scr. Mater.* **2018**, *145*, 23–27. [[CrossRef](#)]

Disclaimer/Publisher's Note: The statements, opinions and data contained in all publications are solely those of the individual author(s) and contributor(s) and not of MDPI and/or the editor(s). MDPI and/or the editor(s) disclaim responsibility for any injury to people or property resulting from any ideas, methods, instructions or products referred to in the content.